Received: 28 June 2023 | Revised: 18 January 2024 | Accepted: 19 January 2024

DOI: 10.1002/asl.1215

RESEARCH ARTICLE

Atmospheric Science Letters RMetS

# The Radon and Hilbert transforms and their applications to atmospheric waves

**Víctor C. Mayta** | **Ángel F. Adames Corraliza** | **Qiao-Jun Lin**

Department of Atmospheric and Oceanic Sciences, University of Wisconsin, Madison, Wisconsin, USA

**Correspondence**
Víctor C. Mayta, Department of Atmospheric and Oceanic Sciences, University of Wisconsin, 1225 West Dayton Street, Madison, WI 53706, USA.
Email: mayta@wisc.edu

**Funding information**
Climate Program Office, Grant/Award Number: NA22OAR4310611; NSF CAREER, Grant/Award Number: 2236433

**Abstract**

The Radon and Hilbert transform and their applications to convectively coupled waves (CCWs) are reviewed. The Hilbert Transform is used to compute the wave envelope, whereas the Radon transform is used to estimate the phase and group velocities of CCWs. Together, they provide an objective method to understand CCW propagation. Results reveal phase speeds and group velocities for fast waves (mixed Rossby-gravity, westward and eastward inertio-gravity, and Kelvin) that are consistent with previous studies and with Matsuno's equatorial wave dispersion curves. However, slowly-propagating tropical depression-like systems and equatorial Rossby waves exhibit wave envelopes that propagate faster than the individual wave crests, which is not predicted by dry shallow water theory.

**KEYWORDS**

atmospheric waves, group velocity, phase speed

## 1 | INTRODUCTION

The phase velocity of any wave indicates its phase propagation, whereas the group velocity indicates the energy dispersion of the wave. Physically, the group velocity represents the propagation speed of wave envelopes. As convectively coupled waves (CCWs) play a crucial role in bridging weather and climate (e.g., Kiladis et al., 2009), it is important to understand both their phase propagation and energy dispersion features.

The Radon transform (RT) is a mathematical technique that is commonly used for image reconstruction and analysis. It was first introduced by Radon (1917) and has since found many applications in various fields including atmospheric sciences. In this field, the RT has been used to calculate the phase speed of oceanic and atmospheric waves. One of the earliest applications of the RT in atmospheric science was in the study of gravity waves by Lindzen and Holton (1968). They used the RT to analyze the phase propagation of atmospheric waves by projecting the wave field onto a series of lines at different angles. By measuring the slope of the resulting projections, they were able to estimate the phase speed of the waves. Since then, the RT has been used in several studies to estimate the phase speed of CCWs (Mayta & Adames, 2021; Mayta et al., 2021; Yang et al., 2007b). In a study by Yang et al. (2007b), the RT was used to investigate the horizontal phase speed of convectively coupled waves. They found that the RT was able to provide accurate estimates of the phase speed even in complex wave fields.

On the other hand, few studies have sought to estimate the group velocity of tropical disturbances. Early studies by Wheeler et al. (2000) estimated the group velocity of CCWs by examining time-longitude diagrams. In Adames and Kim (2016), the authors calculated the

group velocity of the Madden-Julian Oscillation (MJO) in terms of the propagation of the local extrema in the individual wave crests. Later on, Chen and Wang (2018) calculated the wave envelope of the observed MJO-related precipitation anomalies by obtaining the absolute value of the Fourier transform coefficients, as documented by Hayashi (1982).

An alternative way to calculate the wave envelope is through the application of the Hilbert transform (Liu, 2012), a mathematical tool used to calculate the analytic signal associated with a given signal. In atmospheric science, this method has been extensively used to extract key characteristics of mid-latitude transients. For instance, Zimin et al. (2003) pioneered the utilization of the Hilbert transform in the context of mid-latitude Rossby waves. By isolating the analytical signal, the authors were able to identify the distinct properties of Rossby wave packets, such as their amplitude, phase, and spatial–temporal evolution. Subsequent studies (e.g., Souders et al. (2014); Wolf and Wirth (2017); Schoon and Zülicke (2018); among others) further improved the accuracy of Rossby wave packet calculations. In Mayta and Adames (2021), the authors used the Hilbert transform to calculate the wave envelope of two-day waves and understand their coupling to Amazon squall lines (see their fig. 1).

Although the Radon and Hilbert transforms each have distinct advantages in extracting relevant features and analyzing wave propagation patterns, they have not been utilized together to calculate group velocity. The Hilbert transform is a computationally simple tool for wave envelope estimation, while the Radon transform objectively calculates wave propagation. Together, they can provide an objective estimate of phase and group velocities. Thus, the goal of this study is to provide a succinct discussion of the two transforms and showcase their usefulness in studying atmospheric waves. The structure of this paper is as follows: In Section 2, we discuss the data and theoretical basis of the Radon and Hilbert transforms. In Section 3, we examine the methods applied to all convectively coupled waves over the Indo-Pacific warm pool well-documented in Wheeler et al. (2000) and Kiladis et al. (2009). A concluding discussion is offered in Section 4.

## 2 | DATA AND METHODOLOGY

### 2.1 | CLAUS brightness temperature

Satellite-observed brightness temperature ($T_b$) data is used as a proxy for tropical convection. The data is obtained from the Cloud Archive User System (CLAUS) satellite data (Hodges et al., 2000), which has eight-times-daily global fields of $T_b$ from July 1983 to June 2009 and extended through 2018 using the Merged IR dataset from NOAA (see Sakaeda et al. (2020) for more detail). In this study, we use CLAUS data at 4 times daily temporal resolution and $0.5^\circ \times 0.5^\circ$ horizontal resolution. $T_b$ CLAUS data extends from January 1984 through December 2018.

### 2.2 | Wave-type filtering of CLAUS $T_b$

To isolate the signal of CCWs, we used filters based on the Fourier space–time decomposition following the method proposed by Wheeler and Kiladis (1999) and using the same frequency-wavenumber boxes documented in Kiladis et al. (2009). This is accomplished in the wave number-frequency domain by retaining only those spectral coefficients within a specific range corresponding to the spectral peaks associated with a given mode. We also incorporated filters for a specified range of equivalent depth, as indicated in Table 1, for the mixed Rossby-gravity waves (MRGs), eastward inertio-gravity wave (EIG), and westward inertio-gravity wave (WIG). This consideration ensures a clear separation of MRG and EIG signals within the antisymmetric component, as previously outlined by Kiladis et al. (2016). Furthermore, we aim to prevent the mixing of MRG and TD-type signals within the westward propagation domain. MRG waves typically have lower frequencies and have longer zonal wavelengths compared to TD-type. In the case of lower-frequency disturbances, such as Kelvin and equatorial Rossby waves, we do not account for equivalent depth, as these waves encompass a broader range of equivalent depths (Kiladis et al., 2009; Takayabu, 1994; Yang et al., 2007a). The filter settings for the period, the wavenumber $k$, and the equivalent depth $h_e$ are detailed in Table 1.

### 2.3 | Hilbert transform: Calculation of the wave envelope

To study the energy dispersion of the CCWs, the wave envelope $E(\lambda,t)$ is calculated by using the Hilbert transform. This method produces similar results to those obtained following Hayashi's (1982) method, but is arguably more computationally simple. Given a longitude and time-dependent field $f(\lambda,t)$, the wave envelope is obtained via the following formula:

$$E(\lambda,t) = \left| f(\lambda,t) + i\widetilde{f}(\lambda,t) \right|, \quad (1)$$

**TABLE 1** Convectively coupled waves with their corresponding characteristics.

| Acronym | Wave | Period (days) | $k$ | $h_e$ |
|---|---|---|---|---|
| WIG | Westward inertio-gravity | 1.25–3.5 | −15 to −1 | 12–90 |
| EIG | Eastward inertio-gravity | 1–6 | 0–15 | 12–50 |
| MRG | Mixed Rossby-gravity | 2.5–10 | −10 to −1 | 8–90 |
| KW | Kelvin wave | 2.5–20 | 1–15 | – |
| TD | Tropical depression | 2–10 | −20 to −5 | – |
| ER | Equatorial Rossby wave | 10–90 | −20 to 0 | – |

*Note*: The filter settings for the period, wavenumber $k$, and the equivalent depth $h_e$ in meters used to extract the wave signal (see Kiladis et al. (2009) and Kiladis et al. (2016) for more details).

where:

$$\widetilde{f}(\lambda,t)=\frac{1}{\pi}\int_{-\infty}^{\infty}\frac{f(\lambda',t)}{\lambda-\lambda'}d\lambda' \tag{2}$$

is the Hilbert transform in space of $f$. While the real part of Equation (1) is the original time series of the wave, the imaginary is a copy of the original input time series with each of its Fourier components shifted in phase by 90°. This is why the Hilbert transform is often referred to as a 90° phase shifter. Considering that longitude varies between 0 and $\pi$ (Figure 1), we compute the fast Fourier transform (FFT) of the series and keep the complex coefficient, which is much more efficient numerically. Once the wave envelope $E(\lambda,t)$ is computed (represented by the contours in the schematic depiction of Figure 1), we used its time series to calculate the group velocity applying the Radon transform detailed in the next section.

## 2.4 | Radon transform: Calculation of the phase speed ($c_p$) and group velocity ($c_g$)

The Radon transform is employed in this study to calculate phase speed and group velocity given a time-longitude diagram. To better understand this technique, a schematic depiction of the Radon transform is shown in Figure 1. The Radon transform is applied to $f$ for phase speed and to $E$ for group velocity. For the sake of simplicity, the derivation is shown only for the phase speed. Thus, $f(\lambda,t)$ is the integral of $f$ along the line $L$ oriented at angle $\theta$, with a range of angles from 0° to 180°. Thus, the Radon transform is defined as a projection of $f(\lambda,t)$ on $L$ as follows:

$$p(s,\theta)=\int_u f(\lambda,t)du, \tag{3}$$

where $u$ is the direction orthogonal to $L$, and $s$ is the coordinate on $L$. Therefore, for a given $\theta$, the Radon transform is a function of the line coordinate $s$. Rewriting Equation (3) above in terms of coordinates $\lambda$ and $t$,

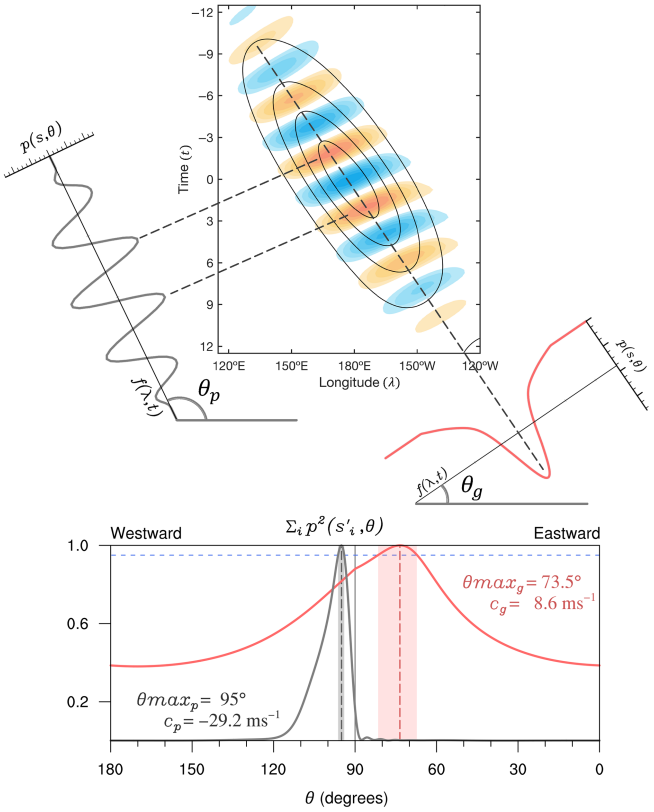


**FIGURE 1** Schematic depicting how the Radon transform is applied to estimate MRG phase speed and group velocity in CLAUS $T_b$. (top) Hovmoller diagram projects onto a plane that has an angle $\theta$ with the $x$-axis. The units for time and longitudes are days and degrees, respectively. (bottom) Density distribution of the sum-of-squares of the Radon transform as a function of projection ($\theta$). The dominant direction with the maximum value equals 1 is marked by a gray dashed line (phase speed) and red dashed line (group velocity). The light red and gray shading represents the uncertainty at a 95% probability of the occurrence of maximum variance.

$$p(\lambda',\theta)=\int_{t'}f(\lambda,t)\left|\begin{Bmatrix}\lambda=\lambda'\cos\theta-t'\sin\theta\\ t=\lambda'\sin\theta+t'\cos\theta\end{Bmatrix}dt' \tag{4}$$

when the lines are perpendicular to the alignment of crests and troughs of the wave (top of Figure 1), the

projection will give the number of image pixels along their projection lines. The zeros of the original and rotated coordinates are where $E$ and $f$ have the maximum amplitude. Therefore the angle ($\theta_p$ and $\theta_g$) perpendicular to that projection gives the direction of propagation of the wave and its dispersion energy in the time-longitude diagram and thus the phase speed and group velocity, respectively. It is worth noting that the magnitude and direction of wave propagation are associated with the maximum variance, which is represented by the dashed lines at the bottom of Figure 1. Furthermore, uncertainty can be incorporated by taking into account a 95% probability of the occurrence of maximum variance, which is represented by the shadings in the schematic figure.

Finally, the phase speed and group velocity is computed by using the value of $\theta$, in which $\int p^2(s,\theta)ds$ is a maximum ($\theta_{\max}$) as follows,

$$c_{p,g} = \frac{2\pi a \cos\phi}{360^\circ} \tan\left(\theta_{\max_{p,g}}\right) \frac{\Delta x}{\Delta t}, \quad (5)$$

where $a$ is the earth's radius and $\frac{2\pi a \cos\phi}{360^\circ}$ is the length of the unit degree at latitude $\phi$. For instance, when the latitude average ranges from 2.5° S to 2.5° N (WIG), gives a value of $\phi = 0^\circ$. $\Delta x$ and $\Delta t$ are the temporal and spatial (°) resolutions of the data grid, respectively.

## 3 | PHASE SPEED AND THE GROUP VELOCITY OF CCWs

Figure 2 gives an example of the application of the combined Hilbert and Radon transforms for MRG and EIG waves. For both waves, we used the base point (7.5° N, 177.5° E), and $T_b$ is averaged for the same latitudes (2.5°–12.5° N) as in Wheeler et al. (2000). To allow comparison with was found in previous studies (e.g., Wheeler et al. (2000); Kiladis et al. (2009)).

Figure 2a shows the longitude–time diagram of $T_b$ of westward-propagating wave signals corresponding to the MRG wave. The contours depict the corresponding longitude–time evolution of the wave envelope. Regressions were computed in a 2.5°–12.5° N range and lag days −10 to +10. To depict the propagation speed of the wave envelope, we applied the RT to the longitude–time diagram of the envelope, as shown in the schematic depiction in Figure 1. The MRG wave moves westward over the Western Pacific at a phase speed of $c_p \approx 29.2$ m s$^{-1}$. This phase speed is obtained from $\theta_{\max_p} = 95.0^\circ$ using Equation (5). An examination of the propagation of the MRG wave envelope yields a value of $\theta_{\max_g} = 73.5^\circ$, which results in an eastward group velocity of $c_g \approx 8.6$ m s$^{-1}$. These results are somewhat different when a line from a longitude–time diagram is used to calculate $c_p$ and $c_g$ (see fig. 12a in Wheeler et al. (2000)). In addition, the phase speed for the MRG waves is slightly different compared to other regions (e.g., Western Hemisphere), where the wave propagates slower (Mayta & Adames, 2023). The propagation features of the MRG vary depending on the basic state, shape, and intensity of the vertical heating profile, as well as the spatial location of the convective heating with respect to the wave dynamical fields (e.g., Yang et al. (2007b)).

The propagation features of the EIG wave are shown in Figure 2b. Compared to MRG waves, EIG waves have a slightly faster phase speed. The RT applied to this disturbance over the western Pacific yields a value of $\theta_{\max_p} = 82.2^\circ$, which results in an eastward phase speed of $c_p \approx 30.5$ m s$^{-1}$. A similar phase speed was also documented in Wheeler et al. (2000) over the same domain (see their fig. 16) and Mayta and Adames (2023) over the

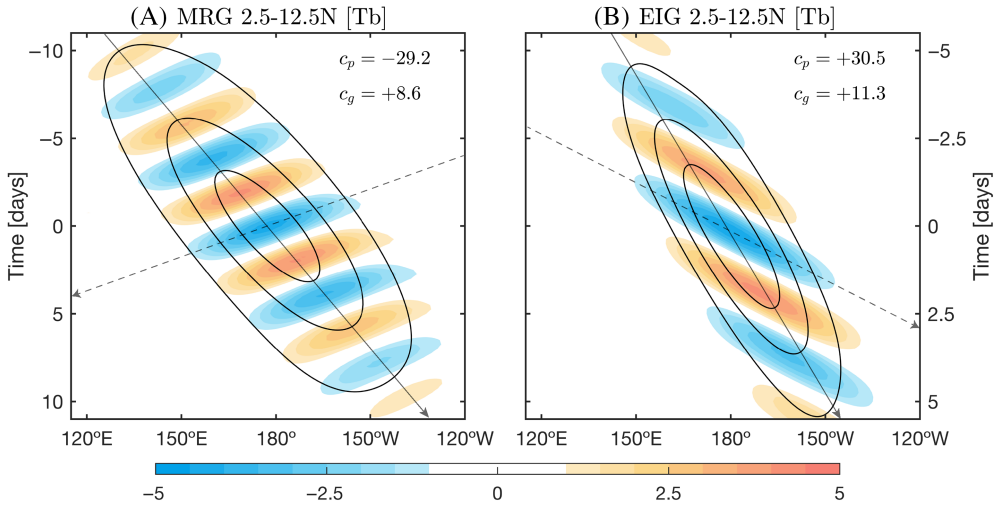


**FIGURE 2** Longitude–time diagram of $T_b$ anomalies (shading) associated with the $T_b$ variation of (a) Mixed Rossby-Gravity waves (MRG) and (b) Eastward Inertial-Gravity waves (EIG) at the base point 7.5° N, 177.5° E. Black contours show the longitude–time evolution of the wave envelope. $T_b$ is averaged for the latitudes of 2.5°–12.5° N. The phase speed ($c_p$, dashed) and group velocity ($c_g$, solid) lines are also shown.

**TABLE 2** Characteristics of convectively coupled waves.

| Wave | Base point | Lat average | $\theta_{\max_p}$ [°] | $c_p$ [m s$^{-1}$] | $\theta_{\max_g}$ [°] | $c_g$ [m s$^{-1}$] |
|---|---|---|---|---|---|---|
| WIG | 0°, 155° E | 2.5° S–2.5° N | 95.0 | −29.3 ± 2.0 | 109.2 | −7.4 ± 5.0 |
| EIG | 7.5° N, 177.5° E | 2.5° N–12.5° N | 82.2 | 30.5 ± 2.9 | 77.3 | 11.3 ± 2.0 |
| MRG | 7.5° N, 177.5° E | 2.5° N–12.5° N | 95.0 | −29.2 ± 3.5 | 73.5 | 8.6 ± 6.3 |
| KW | 0°, 90° E | 5° S–5° N | 79.7 | 14.2 ± 0.8 | 80.3 | 15.1 ± 1.1 |
| TD | 10° N, 100° E | 5° N–15° N | 115 | −7.4 ± 0.8 | 106.3 | −10.5 ± 2.0 |
| ER | 10° S, 150° E | 12.5° S–2.5° S | 121.3 | −4.2 ± 0.7 | 109.8 | −7.1 ± 3.7 |

*Note*: For most CCWs, the base point corresponds to the same as in Wheeler et al. (2000) to allow comparison. The phase speed and group velocity are calculated for the longitude where the wave exhibits significant values. The phase speed ($c_p$) and group velocity ($c_g$) are calculated for the maximum value of the distribution of the sum-of-squares of the RT $\theta_{\max_p}$ and $\theta_{\max_g}$, respectively.

Western Hemisphere. However, as illustrated in Figure 2b, the propagation of the EIG wave envelope is in the same direction as the propagation of the wave. When RT is applied to the envelope yields $\theta_{\max_g} = 77.3°$, which results in an eastward group velocity of $c_g \approx 11.3$ m s$^{-1}$. It is worth noting that the $c_g$ is twice as fast as that found by Wheeler et al. (2000).

The remaining CCWs: Kelvin waves, westward inertial gravity, tropical depression-type (i.e., Easterly Waves), and equatorial Rossby waves were widely documented in previous studies (e.g., Kiladis et al., 2006; Kiladis et al., 2009; Mayta & Adames, 2023; Mayta et al., 2021; Mayta et al., 2022; Wheeler et al., 2000; Yang et al., 2007b; and references therein). Table 2 summarizes the propagation properties of these remaining CCWs. To explore WIG waves, we considered the base point at 0°, 155° E, and $T_b$ is averaged for the latitudes 2.5° S–2.5° N. Over this region, the wave and its corresponding envelope propagate westward over time with $\theta_{\max_p} = 95.0°$ and $\theta_{\max_g} = 109.2°$ giving a $c_p \approx 29.3$ m s$^{-1}$ and $c_g \approx 7.4$ m s$^{-1}$, respectively. Previous studies also documented similar phase speeds for WIG waves over Indo-Pacific region (e.g., Yu et al., 2018). For Kelvin waves, we consider the base point at 0°, 90° E, and $T_b$ is averaged for the latitudes 5° S–5° N. The wave, as in other regions, has an eastward phase speed ranging from 15 to 20 m s$^{-1}$. By using the referred base point and latitudinal average, we found a value of $\theta_{\max_p} = 79.7°$ and $c_p \approx 14.2$ m s$^{-1}$ (Table 2). This is in agreement with previous studies, that show that over the Indian Ocean Kelvin waves propagate slower than in other regions (Mayta et al., 2021; Roundy, 2008; Yang et al., 2007b). As theory suggests, one characteristic feature of the Kelvin wave is that it is non-dispersive, that is, the phase velocity of the wave is equal to the group velocity of the wave energy (Matsuno, 1966). We can see that the wave envelope propagates in the same direction and with almost the same magnitude $\theta_{\max_g} = 80.3°$ and $c_g = 15.1$ m s$^{-1}$.

Slowly-propagating disturbances, such as TD-type waves and equatorial Rossby waves, have complex propagation features (Adames, 2022; Ahmed, 2021; Sobel et al., 2001; Yang et al., 2007b). These features will depend, for instance, on whether the wave is propagating over land or over the ocean, even if it moves over warmer SST or cooler SST conditions (Kiladis et al., 2006; Mayta & Adames, 2023; Vargas Martes et al., 2023). The propagation features of TD-type disturbances over the entire oceanic tropics have recently been documented in Mayta and Adames Corraliza (2023). They found that TD-type waves move westward at phase speeds ranging from 6 to 8 m s$^{-1}$. African easterly waves, which exist over land, have a phase speed of approximately 10 m s$^{-1}$ (Kiladis et al., 2006; Vargas Martes et al., 2023). Here, we used the same base point as in Mayta and Adames Corraliza (2024) over the eastern Pacific (10° N, 100° W) to calculate $c_p$ and $c_g$ of the TD-type wave. For the referred domain, we found a value of $\theta_{\max_p} = 115°$ that yields a $c_p \approx 7.2$ m s$^{-1}$ (Table 2). The wave envelope of TD-like waves propagate in the same direction as the crests but slightly faster ($\theta_{\max_g} = 106.3°$ and $c_g \approx 10.5$ m s$^{-1}$; Figure 3a). The Rossby waves propagation features are showed in Figure 3b. The RT applied to this wave results in $\theta_{\max_p} = 121.3°$ that yields a $c_p \approx 4.2$ m s$^{-1}$ (Table 2). Similar phase speeds were also found in Wheeler et al. (2000), even outside the warm pool Indo-Pacific region (Mayta & Adames Corraliza, 2004; Mayta et al., 2022). The wave envelope, as can be seen as contours in Figure 3b, propagates westward at about $c_g \approx 7.1$ m s$^{-1}$. As occurs in TD-like waves, the results show that $c_g \geq c_p \approx 7.1$ m s$^{-1}$. This implies that the wave envelope propagates almost twice as fast as the wave signal, a feature that has not been previously documented.

We also included uncertainty in the calculation of $c_p$ and $c_g$ (Table 2). It is important to note that the group velocity can vary significantly (e.g., ± 6.3 for MRG waves). As depicted in the schematic Figure 1, the RT

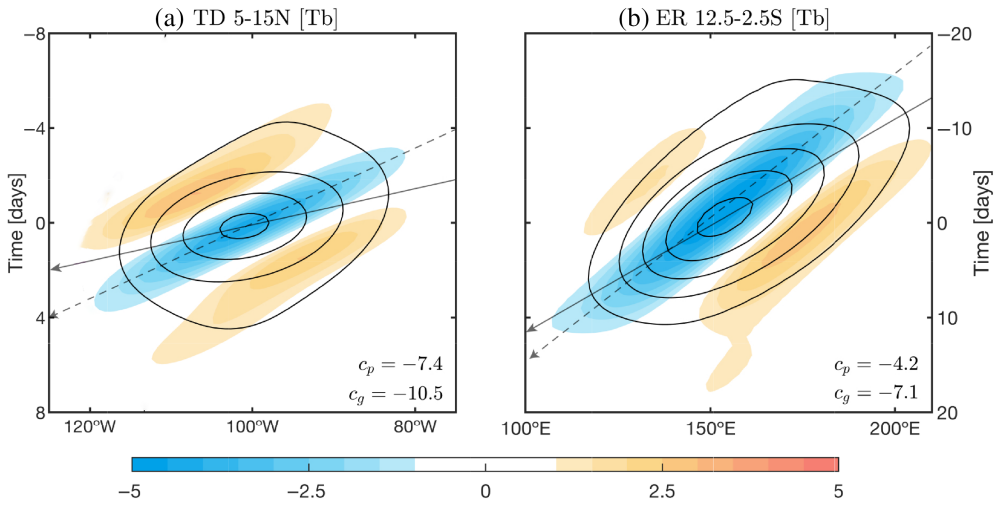


**FIGURE 3** As in Figure 2, but associated with the $T_b$ variation of (a) tropical depression (TD) and (b) equatorial Rossby waves (ER). The base point for TD is 10° N, 100° W and ER 10° S, 150° E. $T_b$ is averaged for the latitudes of 5°–12.5° N and 12.5°–2.5° S for TD and ER, respectively.

approach uses a single envelope to estimate the right $\theta_{\max_g}$ for the group velocity, explaining the wide variations. The opposite occurs with the phase speed. At a 95% probability, there is a narrow variation in $\theta_{\max_p}$ (gray shaded region in Figure 1), indicating a closely clustered distribution around the maximum variance (e.g., ± 0.7 for ER waves). While calculating $c_g$ can be seen as a limitation of this approach, it remains the most accurate method for calculating propagation features.

## 4 | SUMMARY AND CONCLUSIONS

This study reviews the calculation of phase speed and group velocity of Convectively Coupled Waves (CCWs). We applied the combined Hilbert and Radon transforms to analyze the wave propagation characteristics. To allow comparison with previous methods, which have been widely documented in previous studies, we used the same basis points and domains documented in Wheeler et al. (2000).

For mixed Rossby-gravity waves (MRG), we found a westward phase speed of ∼29.2 m s$^{-1}$ and an eastward group velocity of ∼8.6 m s$^{-1}$ (Figure 2a). The phase speed of MRG waves, however, can varies depending on the region (e.g., Mayta & Adames, 2023; Yang et al., 2007b). The propagation features of eastward inertio-gravity waves (EIG) are also examined, revealing a slightly faster phase speed of ∼30.5 m s$^{-1}$ and an eastward group velocity of ∼11.3 m s$^{-1}$ (Figure 2b).

WIG waves exhibit a westward phase speed of ∼29.3 m s$^{-1}$ and a westward group velocity of ∼7.4 m s$^{-1}$. Similar propagation features were also found in Wheeler et al. (2000), even in other regions such as the Amazon Basin (Mayta & Adames, 2021). Kelvin waves have an eastward phase speed ranging from 15 to 20 m s$^{-1}$, and the wave envelope propagates in the same direction and with the same magnitude of the phase speed (i.e., as a non-dispersive wave). Overall, Kelvin, MRG, and WIG waves exhibit phase speeds and group velocities that are consistent with shallow-water dry theory with "reduced" equivalent depths that account for convective coupling (Kiladis et al., 2009).

It is well known that midlatitude Rossby waves exhibit $|c_g| > |c_p|$, a result that can be readily obtained from the Rossby wave dispersion relation under the presence of mean westerly winds (Chang (1993); Grimm and Dias (1995); Fragkoulidis and Wirth (2020); among others). In the tropics, the mean winds are usually easterlies. Using dry theory, one would obtain $|c_g| < |c_p|$ in equatorial Rossby waves (see Appendix for a detailed derivation of $c_g$). Equatorial Rossby waves exhibit a westward phase speed of ∼4.2 m s$^{-1}$ and a group velocity of 7.1 m s$^{-1}$. Thus, $|c_g| > |c_p|$ in equatorial Rossby waves (see Figure 3) and therefore do not follow dry theory (Figure 3).

Similarly, TD-type waves showed a westward phase speed of ∼7.2 m s$^{-1}$, in agreement with recent works that found a phase speed ranging from 6 to 8 m s$^{-1}$ (Mayta & Adames Corraliza, 2024). Their group velocity is 10.5 m s$^{-1}$. Thus, $|c_g| > |c_p$ in these waves as well. TD-type waves do not exist in Matsuno's theory, but are sometimes thought of as a type of Rossby wave (see chapter 9 in Riehl (1954)), in which case the same arguments of the equatorial Rossby wave would apply. Hence, dry theory is unable to explain the propagation characteristics of neither equatorial Rossby or TD-type waves. These results highlight the limitations of dry theory when applied to these waves. Moisture mode theory (Adames, 2022; Adames & Maloney, 2021; Mayta & Adames Corraliza, 2024; Mayta et al., 2022; Sobel

et al., 2001) may be a more reasonable starting point to understand the propagation features of these waves.

## AUTHOR CONTRIBUTIONS

**Víctor C. Mayta**: Study conception and design; analysis and interpretation of results; and manuscript preparation. **Angel Adames-Corraliza:** Conceptualization; investigation; supervision; writing – review and editing. **Qiao-Jun Lin:** Formal analysis; methodology.

## ACKNOWLEDGEMENTS

VM and ÁFAC was also supported by NOAA grant number NA22OAR4310611 and NSF CAREER grant number 2236433.

## FUNDING INFORMATION

This research was funded by NOAA grant number NA22OAR4310611.

## CONFLICT OF INTEREST STATEMENT

The authors declare no conflicts of interest.

## DATA AVAILABILITY STATEMENT

The data that support the findings of this study are available on request from the corresponding author, VM.

## ORCID

*Víctor C. Mayta* https://orcid.org/0000-0003-4037-1722
*Ángel F. Adames Corraliza* https://orcid.org/0000-0003-3822-5347
*Qiao-Jun Lin* https://orcid.org/0000-0003-4539-2688

## REFERENCES

Adames, Á.F. (2022) The basic equations under weak temperature gradient balance: formulation, scaling, and types of convectively-coupled motions. *Journal of the Atmospheric Sciences*, 74, 1799–1817.

Adames, Á.F. & Kim, D. (2016) The MJO as a dispersive, convectively coupled moisture wave: theory and observations. *Journal of the Atmospheric Sciences*, 73, 913–941.

Adames, Á.F. & Maloney, E.D. (2021) Moisture mode theory's contribution to advances in our understanding of the Madden-Julian oscillation and other tropical disturbances. *Current Climate Change Reports*, 7, 72–85. Available from: https://doi.org/10.1007/s40641-021-00172-4

Ahmed, F. (2021) The MJO on the equatorial beta plane: an eastward-propagating Rossby wave induced by meridional moisture advection. *Journal of the Atmospheric Sciences*, 78, 3115–3135.

Chang, E.K.M. (1993) Downstream development of baroclinic waves as inferred from regression analysis. *Journal of Atmospheric Sciences*, 50, 2038–2053.

Chen, G. & Wang, B. (2018) Does the MJO have a westward group velocity? *Journal of Climate*, 31, 2435–2443.

Fragkoulidis, G. & Wirth, V. (2020) Local Rossby wave packet amplitude, phase speed, and group velocity: seasonal variability and their role in temperature extremes. *Journal of Climate*, 33, 8767–8787.

Grimm, A.M. & Dias, P.L.S. (1995) Analysis of tropical–extratropical interactions with influence functions of a barotropic model. *Journal of Atmospheric Sciences*, 52, 3538–3555.

Hayashi, Y. (1982) Space-time spectral analysis and its applications to atmospheric waves. *Journal of the Meteorological Society of Japan. Series II*, 60, 156–171.

Hodges, K.I., Chappell, D.W., Robinson, G.J. & Yang, G. (2000) An improved algorithm for generating global window brightness temperatures from multiple satellite infrared imagery. *Journal of Atmospheric and Oceanic Technology*, 17, 1296–1312.

Kiladis, G.N., Dias, J. & Gehne, M. (2016) The relationship between equatorial mixed Rossby–gravity and eastward inertio-gravity waves. Part I. *Journal of the Atmospheric Sciences*, 73, 2123–2145.

Kiladis, G.N., Thorncroft, C.D. & Hall, N.M.J. (2006) Three-dimensional structure and dynamics of African easterly waves. Part I: observations. *Journal of the Atmospheric Sciences*, 63, 2212–2230.

Kiladis, G.N., Wheeler, M.C., Haertel, P.T., Straub, K.H. & Roundy, P.E. (2009) Convectively coupled equatorial waves. *Reviews of Geophysics*, 47, RG2003.

Lindzen, R.S. & Holton, J.R. (1968) A theory of the quasi-biennial oscillation. *Journal of the Atmospheric Sciences*, 25, 1095–1107. Available from: https://doi.org/10.1175/1520-0469(1968)025<1095:ATOTQB>2.0.CO;2

Liu, Y.-W. (2012) Hilbert transform and applications. In *Fourier transform applications*. London: IntechOpen, pp. 291–300.

Matsuno, T. (1966) Quasi-geostrophic motions in the equatorial area. *Journal of the Meteorological Society of Japan*, 44, 25–43.

Mayta, V.C. & Adames, A.F. (2021) Two-day westward-propagating inertio-gravity waves during GoAmazon. *Journal of the Atmospheric Sciences*, 78, 3727–3743.

Mayta, V.C. & Adames, Á.F. (2023) Moist thermodynamics of convectively coupled waves over the western hemisphere. *Journal of Climate*, 36, 2765–2780.

Mayta, V.C., Adames, Á.F. & Ahmed, F. (2022) Westward-propagating moisture mode over the tropical Western hemisphere. *Geophysical Research Letters*, 49, e2022GL097799.

Mayta, V.C. & Adames Corraliza, Á.F. (2024) The stirring tropics: the ubiquity of moisture modes and moisture-vortex instability. *Journal of Climate*, in press. https://doi.org/10.1175/JCLI-D-23-0145.1

Mayta, V.C., Kiladis, G.N., Dias, J., Dias, P.L.S. & Gehne, M. (2021) Convectively coupled kelvin waves over tropical South America. *Journal of Climate*, 34, 1–52.

Radon, J. (1917) Über die Bestimmung von Funktionen durch ihre Integralwerte längs gewisser Mannigfaltigkeiten. *Akademie der Wissenschaften*, 69, 262–277.

Riehl, H. (1954) *Tropical meteorology*. New York: McGrawhill, p. 392.

Roundy, P.E. (2008) Analysis of convectively coupled Kelvin waves in the Indian ocean MJO. *Journal of the Atmospheric Sciences*, 65, 1342–1359.

Sakaeda, N., Kiladis, G. & Dias, J. (2020) The diurnal cycle of rainfall and the convectively coupled equatorial waves over the maritime continent. *Journal of Climate*, 33, 3307–3331.

Schoon, L. & Zülicke, C. (2018) A novel method for the extraction of local gravity wave parameters from gridded three-dimensional data: description, validation, and application. *Atmospheric Chemistry and Physics*, 18, 6971–6983.

Sobel, A.H., Nilsson, J. & Polvani, L.M. (2001) The weak temperature gradient approximation and balanced tropical moisture waves. *Journal of the Atmospheric Sciences*, 58, 3650–3665.

Souders, M.B., Colle, B.A. & Chang, E.K.M. (2014) The climatology and characteristics of Rossby wave packets using a feature-based tracking technique. *Monthly Weather Review*, 142, 3528–3548.

Takayabu, Y.N. (1994) Large-scale cloud disturbances associated with equatorial waves. Part I: spectral features of the cloud disturbances. *Journal of the Meteorological Society of Japan*, 72, 433–449.

Vargas Martes, R., Adames Corraliza, Á.F. & Mayta, V.C. (2023) The role of water vapor and temperature in the thermodynamics of tropical Northeast Pacific and African easterly waves. *Journal of the Atmospheric Sciences*, 80, 2305–2322.

Wheeler, M. & Kiladis, G. (1999) Convectively-coupled equatorial waves: analysis of clouds in the wavenumber-frequency domain. *Journal of the Atmospheric Sciences*, 56, 374–399.

Wheeler, M.C., Kiladis, G.N. & Webster, P.J. (2000) Largescale dynamical fields associated with convectively coupled equatorial waves. *Journal of the Atmospheric Sciences*, 57, 613–640.

Wolf, G. & Wirth, V. (2017) Diagnosing the horizontal propagation of Rossby wave packets along the midlatitude waveguide. *Monthly Weather Review*, 145, 3247–3264.

Yang, G.-Y., Hoskins, B. & Slingo, J. (2007a) Convectively coupled equatorial waves. Part I: horizontal and vertical structures. *Journal of the Atmospheric Sciences*, 64, 3406–3423.

Yang, G.-Y., Hoskins, B. & Slingo, J. (2007b) Convectively coupled equatorial waves. Part II: propagation characteristics. *Journal of the Atmospheric Sciences*, 64, 3424–3437.

Yu, H., Johnson, R.H., Ciesielski, P.E. & Kuo, H.-C. (2018) Observation of quasi-2-day convective disturbances in the equatorial Indian ocean during dynamo. *Journal of the Atmospheric Sciences*, 75, 2867–2888.

Zimin, A.V., Szunyogh, I., Patil, D.J., Hunt, B.R. & Ott, E. (2003) Extracting envelopes of Ross by wave packets. *Monthly Weather Review*, 131, 1011–1017.

**How to cite this article:** Mayta, V. C., Adames Corraliza, Á. F., & Lin, Q.-J. (2024). The Radon and Hilbert transforms and their applications to atmospheric waves. *Atmospheric Science Letters*, *25*(5), e1215. https://doi.org/10.1002/asl.1215

# APPENDIX

## DRY ROSSBY WAVE DISPERSION

We begin with Matsuno's dispersion for equatorial Rossby waves, with the inclusion of a constant zonal flow:

$$\omega = \overline{u}k - \frac{\beta k}{k^2 + \underbrace{(2n+1)R_d^{-2}}_{l_d^2}}. \tag{A.1}$$

From the dispersion relationship shown in Equation (A.1), the phase speed of the equatorial Rossby waves can be written as follows:

$$c_p = \overline{u} - \frac{\beta}{k^2 + l_d^2}. \tag{A.2}$$

If $\overline{u}$ is westward, it follows that $c_p$ will always be negative and the wave propagates at a speed that is slightly faster than the zonal mean flow.

The group velocity ($c_g \equiv \partial\omega/\partial k$) describes the movement of the wave envelope shown in Figures 1 and 3:

$$c_g = \frac{\partial}{\partial k}\left(\overline{u}k - \frac{\beta k}{k^2 + l_d^2}\right) = \overline{u} - \frac{\beta\left(l_d^2 - k^2\right)}{\left(k^2 + l_d^2\right)^2}. \tag{A.3}$$

Using Equation (A.2) we can write the group velocity in terms of the phase speed:

$$c_g = c_p + \frac{\beta}{k^2 + l_d^2} - \frac{\beta\left(l_d^2 - k^2\right)}{\left(k^2 + l_d^2\right)^2}. \tag{A.4}$$

If we combine the last two terms on the right-hand side we arrive at the following relation:

$$c_g = \underbrace{c_p}_{west} + \underbrace{\frac{2\beta}{\left(k^2 + l_d^2\right)^2}}_{east}. \tag{A.5}$$

Hence, since the two terms in Equation (A.5) are of opposite signs, it follows that $c_g$ should be smaller than $c_p$. This result is inconsistent with the observations shown in Figure 3, which shows that $c_g$ is faster than $c_p$.